

# Temperature-controlled vacuum quenching for perovskite solar modules towards scalable production

Received: 19 September 2024

Accepted: 12 May 2025

Published online: 25 June 2025

 Check for updates

Leyu Bi<sup>1,2</sup>, Jiarong Wang<sup>2,3</sup>, Zixin Zeng<sup>3</sup>, Xiaofei Ji<sup>4</sup>, Xiaofeng Huang<sup>1,2</sup>, Francis R. Lin<sup>1,2,3</sup>, Sai-Wing Tsang<sup>3</sup>, Qiang Fu<sup>1,2,3</sup>✉ & Alex K.-Y. Jen<sup>1,2,3</sup>✉

Perovskite solar cells (PSCs) exhibit substantially improved performance and stability; however, maintaining high power conversion efficiency (PCE) and stability while up-scaling cell areas remains challenging. Furthermore, perovskite nucleation and growth are highly sensitive to processing methods, increasing the complexity of large-scale production. To address these challenges, we establish a temperature-controlled vacuum quenching method combined with in situ photoluminescence spectrometry to fabricate perovskite films under monitoring. We systematically study the commonly used quenching nucleation processes and reveal the impact of the pumping speed, solvent system and additives on the vacuum quenching process. We manage to modulate the perovskite nucleation process by lowering the temperature during the vacuum quenching process, thereby broadening the time window for post-processing treatments to obtain high-quality large-area perovskite films. The resultant 1.55 eV mini-module achieves a PCE of 22.69% with an aperture area of 11.7 cm<sup>2</sup> (and a certified aperture-area PCE of 21.60%), whereas the corresponding PSC maintained >93% of its initial efficiency after continuously operating at 45 °C for 3,500 h under 1 sun illumination. This approach enables high-quality, uniform and large-area perovskite films on rigid, flexible and curved substrates, demonstrating the feasibility of our strategy for improving the scalability of renewable PSC technology.

Perovskite solar cells (PSCs) have witnessed remarkable advancement, encompassing manufacturing techniques such as slot-die coating and vacuum quenching (VAQ)<sup>1–4</sup>. Nevertheless, a disparity persists in the efficiency of perovskite solar modules (PSMs) versus the cell efficiency<sup>4,5</sup>. It is well established that the nucleation and growth of perovskites exhibit high sensitivity to processing methods, which is exacerbated in large-scale production<sup>6,7</sup>. Any minute deviation from the optimal conditions can give rise to defects and non-uniformity,

resulting in a deterioration in the performance and stability of the resultant perovskite films<sup>8,9</sup>.

A critical factor in achieving large-scale and economically feasible production of PSCs is to upscale the film formation process to large areas through scalable deposition techniques<sup>10–12</sup>. It is now widely acknowledged that rapid drying induced by antisolvent<sup>13</sup>, vacuum<sup>14,15</sup> or gas quenching<sup>16,17</sup> can considerably enhance the morphology of perovskite films<sup>18,19</sup>. The commonality among these rapid drying methods

<sup>1</sup>Department of Chemistry, City University of Hong Kong, Kowloon, China. <sup>2</sup>Hong Kong Institute for Clean Energy (HKICE), City University of Hong Kong, Kowloon, China. <sup>3</sup>Department of Materials Science and Engineering, City University of Hong Kong, Kowloon, China. <sup>4</sup>Shanghai Advanced Research Institute Chinese Academy of Sciences, Shanghai, China. ✉e-mail: [qfu222@cityu.edu.hk](mailto:qfu222@cityu.edu.hk); [alexjen@cityu.edu.hk](mailto:alexjen@cityu.edu.hk)

is that they facilitate rapid nucleation of films by rapidly altering environmental parameters<sup>9,20</sup>. Meticulous monitoring and control of the film formation stages (that is, drying, nucleation and crystal growth) are necessary to obtain high-quality optoelectronic films; however, one current challenge lies in our lack of profound understanding of the physical processes during the drying of solution films and the formation of associated perovskite films<sup>21</sup>. In situ characterization is therefore a good tool that can be used to gain insights into the complex fabrication process of perovskite films<sup>22–24</sup>.

Another notable challenge is identifying an efficient approach to control the nucleation and growth of perovskites in large-scale manufacturing processes to maintain high power conversion efficiency (PCE)<sup>25,26</sup>. The complexity involved in optimizing multiple process parameters such as drying methods, solvent systems, temperature and additives presents an important impediment to obtaining uniform and high-quality perovskite films<sup>27,28</sup>. Developing a scalable and cost-effective method for producing high-quality, uniform perovskite films on various substrates—including rigid and flexible ones—is therefore essential for the widespread application of PSCs in the real world.

Herein we propose a temperature-controlled vacuum quenching (T-VAQ) nucleation approach for the solution-based fabrication of perovskite films. This innovative methodology is devised to tackle the challenges associated with large-scale production of high-quality perovskite films. First, we systematically investigated three commonly used quenching nucleation processes by integrating the in situ photoluminescence. We then deciphered the influences of pumping speed, solvent system and additives on the vacuum quenching process. The in-depth analysis enabled us to comprehensively understand the underlying mechanisms and optimize the process parameters for superior performance. Equally important, the intermediate phase can be prolonged by regulating vacuum quenching at a lower temperature (10 °C), thereby extending the time window for post-treatment. The resulting 1.55 eV inverted PSCs achieved a PCE of 25.50%. The resulting wide-bandgap (1.67 eV) PSCs also showed an encouraging PCE of 22.14%; it also yielded a mini-module with an aperture area of 11.7 cm<sup>2</sup> and a high PCE of 22.69% (certified aperture-area PCE of 21.60%). Moreover, the PSCs using T-VAQ maintained >93% of initial efficiency in long-term operational stability tests under 45 °C for 3,500 h. This method facilitates the acquisition of high-quality, uniform and large-area perovskite films on rigid, flexible and curved substrates, holding substantial promise for the future of perovskite solar cells and potentially accelerating their integration into mainstream energy production systems.

## Result and discussion

### In situ monitoring of quenching and nucleation processes

The schematic diagram of the production process of perovskite solar modules illustrates the diverse steps (Fig. 1a) encompassing functional layer deposition, perovskite film deposition, electrode evaporation and laser patterning. Among these, perovskite film deposition is a distinctive step specifically developed for the perovskite photovoltaic industry<sup>29</sup>. Uniform and dense perovskite films with high crystallinity are essential to achieve adequate light absorption and facilitate charge transfer<sup>30,31</sup>. However, spin-coating combined with anti-solvent quenching, which is commonly used for small-area PSCs, remains a substantial challenge in obtaining high-quality large-area perovskite films<sup>13,32</sup>. Thus, various solution deposition and drying techniques have recently been developed, enabling high-throughput manufacturing and precise control over the stoichiometric ratio of perovskite films<sup>33</sup>.

As shown in Fig. 1b, the basic processing steps of the solution deposition are mainly: (1) coating (deposition of the precursor film); (2) quenching and nucleation (the solvent is transported out of the film, and nuclei are uniformly formed through supersaturation); and (3) annealing and crystal growth (that is, the growth and ripening of perovskite crystals)<sup>2</sup>. Here we use the in-house constructed in situ

photoluminescence equipment to monitor the changes in the perovskite precursor films prepared by different coating and quenching methods such as anti-solvent, vacuum and gas quenching (Fig. 1c and Supplementary Fig. 1). These results can reveal the mechanisms and influencing factors of different quenching methods, which can guide the drying, nucleation and crystallization processes of high-quality perovskite layers and help improve the understanding of the scalable manufacturing of perovskite layers.

### Comparison of three mainstream quenching nucleation methods

As shown in Fig. 2a–c, for the spin-coated samples, the appearance time of the PL<sub>max</sub> signal in the photoluminescence thermogram treated by the antisolvent, vacuum or gas quenching nucleation methods are delayed successively, indicating that the quenching and nucleation abilities of these three methods decrease in turn (antisolvent > vacuum > gas). Moreover, the blade-coated samples also showed the same trend under the three drying methods (Fig. 2d–f). Furthermore, the line graph extracted from the photoluminescence thermogram further confirmed this conclusion (Fig. 2g,h). Interestingly, the photoluminescence intensity of the precursor film treated by vacuum clearly exhibited a step phenomenon as the treatment time increased (Fig. 2g,h and Supplementary Fig. 2), indicating that the precursor film formed a particular intermediate phase. The photoluminescence intensity of the samples treated by antisolvent drip or immersion showed a trend of rapid enhancement and decline (Fig. 2h), possibly because the quenching speed is too fast and the intermediate phase cannot exist stably. Furthermore, the film morphology and X-ray diffraction (XRD) after different quenching methods (Supplementary Fig. 3), and scanning electron microscopy (SEM) and XRD after annealing (Supplementary Figs. 4 and 5), can also prove that vacuum quenching has faster nucleation characteristics than gas quenching. Vacuum quenching's nucleation characteristics are more controllable than anti-solvent quenching, and the perovskite precursor formula suitable for anti-solvent quenching can also be directly transplanted into the vacuum quenching method to obtain better perovskite films. Based on the above results and analysis, we summarize the advantages and disadvantages of these three commonly used quenching methods from five aspects (Fig. 2i and Supplementary Table 1). Among them, the vacuum quenching method has unique advantages in device repeatability and environmental friendliness compared to the other two quenching methods<sup>20</sup>.

### Deciphering the process of vacuum quenching nucleation

Based on the research above, vacuum quenching holds remarkable potential for preparing high-quality large-area perovskite films. Nevertheless, the mechanism and process of vacuum nucleation have garnered limited research focus. By integrating with past reports<sup>9,20</sup>, we have classified the perovskite nucleation process in vacuum quenching into three stages.

In the first stage (Fig. 3a), the vacuum mainly removes the gas within the chamber. The law governing the variation of the system pressure over time can be presented as follows:

$$P(t) = P(0)e^{-\frac{S}{V}t}$$

Here,  $S$  is the pumping speed,  $V$  is the volume of the chamber and  $t$  is the pumping duration. This function could indicate the chamber pressure after pumping for a specific duration (refer to Supplementary Information for more details). The measured pressure data corresponding to this function is shown in Fig. 3b. In this stage, a higher vacuum pumping speed will accelerate the nucleation process of the perovskite precursor (Fig. 3b,c and Supplementary Fig. 6).

In the second stage (Fig. 3d), the vacuum removes the solvent molecules within the film and the residual gas in the vacuum chamber. During this process, the solvent with a lower boiling point evaporates

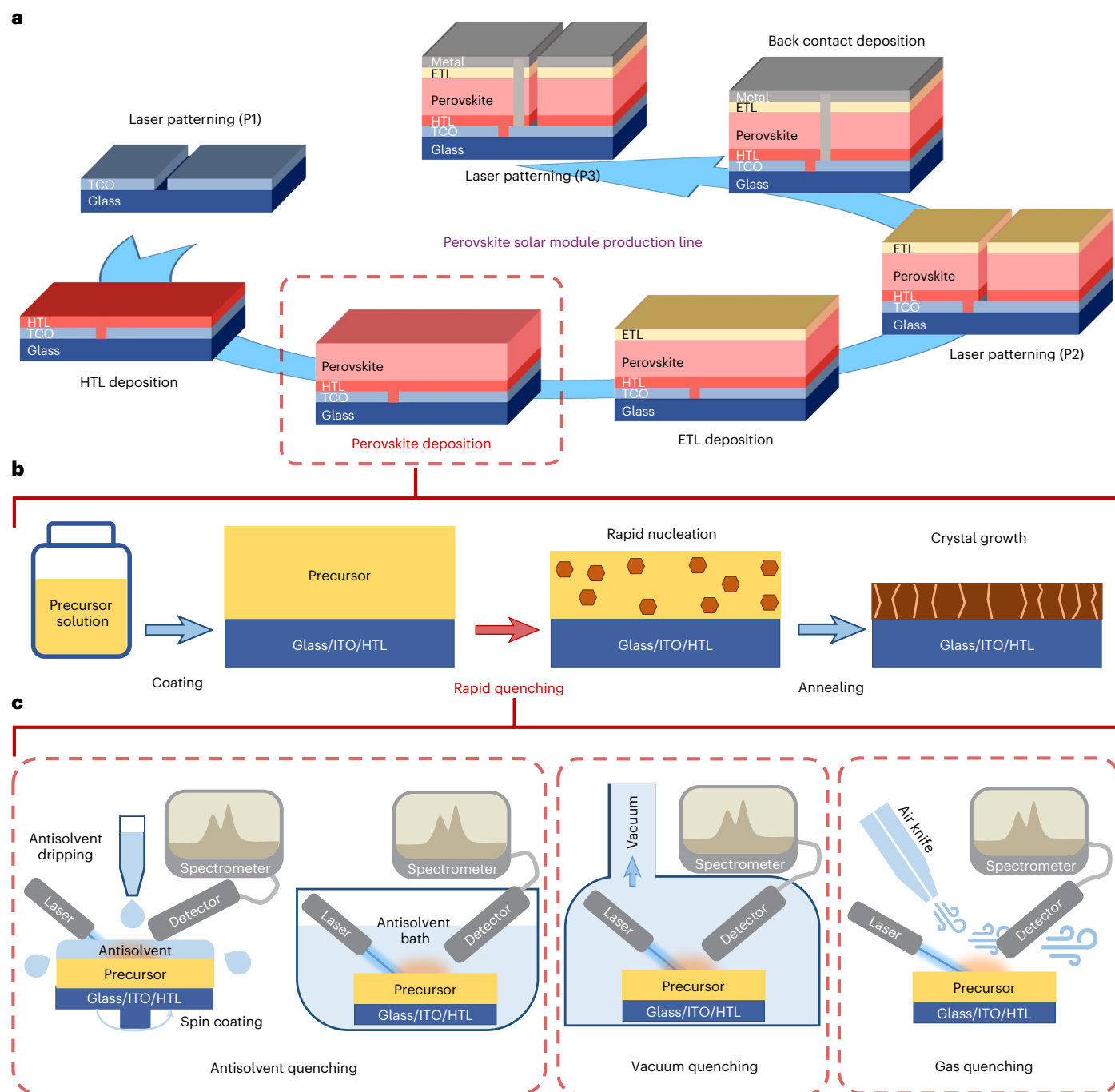


**Fig. 1 | In situ monitoring of quenching and nucleation processes.** **a**, Schematic diagram of the production process of perovskite solar modules. Compared with electrode evaporation, functional layer deposition and laser patterning process, perovskite film deposition (marked by a red dashed box) is a unique step developed only for the perovskite photovoltaic industry. **b**, Three key steps in the perovskite deposition by the solution-processable method (the coating of

precursor solution, rapid quenching nucleation and the crystal growth process via annealing). **c**, Schematic diagram of the mainstream quenching methods, including anti-solvent, vacuum and gas quenching, which is monitored by in situ photoluminescence. HTL, hole transport layer; ETL, electron transport layer; TCO, transparent conductive oxide.

more quickly, or in other words, evaporates at higher pressure (Fig. 3e and Supplementary Figs. 7 and 8). The specific solvent boiling points at different vacuum pressures are determined by Antoine's law, Raoult's law and the activity coefficients of the solvent (Supplementary Information, Supplementary Fig. 7, and Supplementary Tables 2 and 3)<sup>34</sup>. Specifically, when compared with the curve without a solvent, the *N,N*-dimethylformamide (DMF) curve began to increase at around 300 mTorr, dimethyl sulfoxide (DMSO) was approximately 100 mTorr, and *N*-methylpyrrolidone (NMP) exhibited a notable change at about

70 mTorr. We then conducted the in situ photoluminescence study of the precursor film with different solvent systems and found that the above law holds where low-boiling-point solvents will accelerate nucleation (Fig. 3f and Supplementary Fig. 9).

In the third stage (Fig. 3g), the vacuum continues to extract the solvent molecules; however, the interaction between the solvent and the solute cannot be ignored. At this stage of the process, the solution reaches supersaturation and commences nucleation. Solvents that have stronger interactions with the solute will be more challenging to extract,

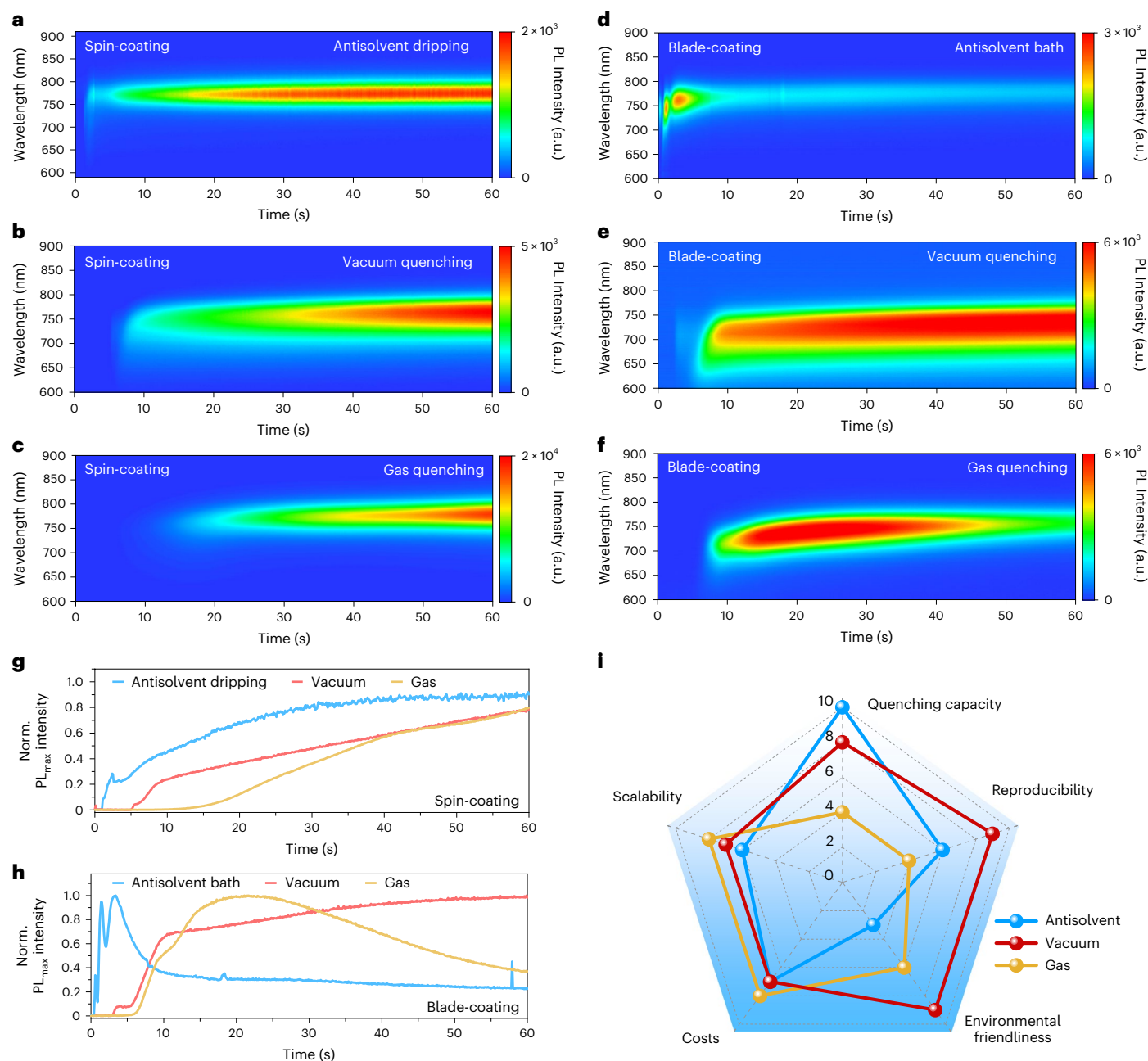


**Fig. 2 | Comparison of three mainstream quenching nucleation methods.** **a–c**, In situ photoluminescence heat maps of the nucleation process using spin-coating based on a DMF:DMSO solvent system during anti-solvent dripping (**a**), vacuum quenching (**b**) and gas quenching (**c**). **d–f**, In situ photoluminescence heat maps of the nucleation process using blade-coating based on DMF:NMP solvent system during an anti-solvent bath (**d**), vacuum quenching (**e**) and gas

quenching (**f**). **g,h**, The maximum peak intensity of in situ photoluminescence versus time during different quenching processes using spin- (**g**) or blade-coating (**h**). **i**, A radar map comparing the three nucleation methods through five different measures: quenching capacity, reproducibility, environmental friendliness, costs and scalability. PL, photoluminescence.

such as DMSO (29.8), which has a higher donor number than NMP (27.3), which will in turn delay nucleation (Fig. 3h and Supplementary Fig. 10). The donor numbers of the common solvents used for precursors are also summarized in Supplementary Table 3. Aside from the solvents, different additives will also impact the nucleation process. For example, the photoluminescence intensity of the precursor film with methylammonium chloride (MACl) during vacuum treatment is higher than that of the control film (Fig. 3i), indicating that MACl effectively increases pre-nucleation and produces more nucleation sites<sup>21</sup>. Furthermore, during vacuum treatment, the in situ photoluminescence curve of the precursor film with 4-fluoro-phenethylammonium iodide (*p*-F-PEAI) seems shorter, indicating that *p*-F-PEAI promotes faster nucleation (Fig. 3i and

Supplementary Fig. 11). Vacuum quenching nucleation also applies to producing wide-bandgap (1.79 eV) perovskites (Supplementary Fig. 12). Based on this research, we have identified the factors influencing the pumping speed, solvent system and additives in the three stages of vacuum quenching. This has guided suggestions for the subsequent comprehensive design of the equipment and the perovskite precursor solution system to realize high-quality perovskite film.

### Temperature-controlled vacuum quenching

In addition to the perovskite components, solvents and vacuum treatment equipment, the ambient temperature also substantially influences the nucleation process during the drying process of perovskite films<sup>35</sup>.

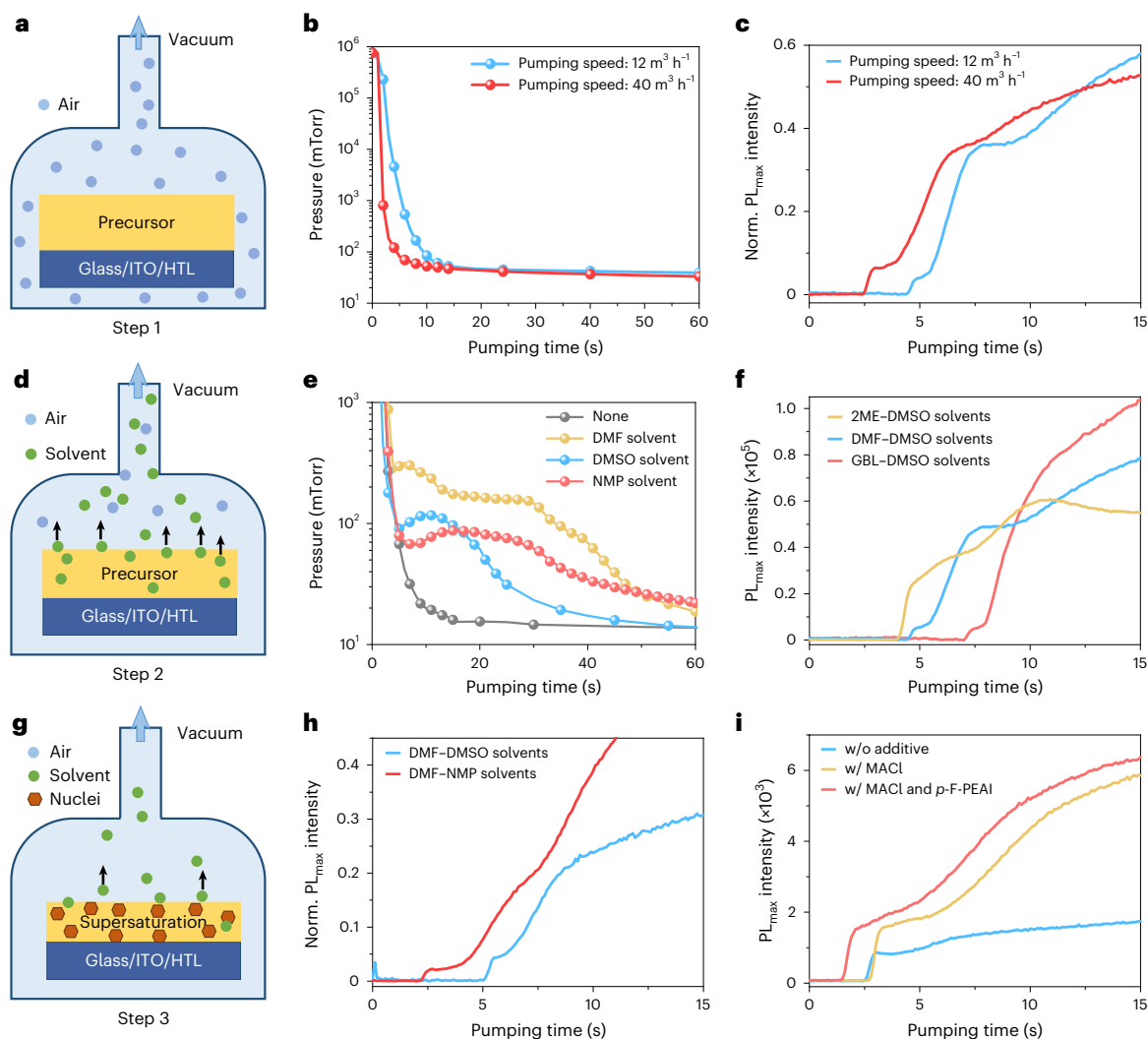


**Fig. 3 | Deciphering the process of vacuum quenching nucleation.** **a**, Schematic diagram of the first stage of vacuum quenching. The air pressure in the vacuum chamber is high at this stage, and only the air in the vacuum chamber is pumped out. **b**, A pressure–pumping curve showing how the pressure in the vacuum chamber changes over time when a vacuum pump with different pumping speeds is used to evacuate the chamber. **c**, The maximum peak intensity of in situ photoluminescence versus pumping time with different pumping speeds. **d**, Schematic diagram of the second stage of vacuum quenching. The solvent in the precursor film begins to evaporate in this stage; however, it is far from reaching saturation, which is equivalent to solvent volatilization. **e**, A pressure–pumping curve showing how the pressure in the vacuum chamber

changes over time when solvent droplets with different boiling points are added. **f**, The maximum peak intensity of in situ photoluminescence versus pumping time when the primary solvents with different boiling points are used in the precursor. 2-ME, 2-methoxyethanol; GBL,  $\gamma$ -butyrolactone. **g**, Schematic diagram of the third stage of vacuum quenching. The solute in the precursor film is close to saturation and rapidly nucleates at this stage, and the removal of the solvent will produce an interaction with the solute. **h**, The maximum peak intensity of in situ photoluminescence versus pumping time when Lewis base solvents with different binding energies are used in the precursor. **i**, The maximum peak intensity of in situ photoluminescence versus pumping time when different additives are used in the precursor.

As shown in Supplementary Fig. 13, we found that the temperature of the precursor film immediately dropped by 6 °C during the antisolvent quenching process after the antisolvent was added. This dynamic change introduces more challenges to the nucleation process of the antisolvent; however, the temperature change of the precursor film during the vacuum treatment was minimal (Supplementary Fig. 13), indicating the higher controllability of the vacuum treatment. We built a T-VAQ platform with integrated in situ photoluminescence monitoring to more precisely control the temperature during the vacuum quenching nucleation process. The perovskite substrate placed on the T-VAQ platform can reach a temperature similar to the platform within 2 s (Supplementary Fig. 14). We can therefore ignore the temperature change during the vacuum quenching process and attribute the difference in the nucleation process to the change in the preset equipment temperature.

We monitored the nucleation process at different temperatures using in situ photoluminescence to unravel the impact of temperature on the nucleation process (Fig. 4g). The photoluminescence heat maps (Fig. 4a–c) show that the film nucleation signal weakens at lower temperatures. From the wavelength and intensity change extracted from the heat map (Fig. 4d and Supplementary Figs. 15 and 16), the lower the ambient temperature, the longer it takes to reach the same nucleation process. For example, at ambient temperatures of 10 °C, 20 °C and 30 °C, the time required for the wavelength of the PL<sub>max</sub> peak of the sample to change from 680 nm to 720 nm is 38 s, 12 s and 4 s, respectively (Supplementary Table 4). This result shows that low temperature considerably slows the perovskite nucleation speed and broadens the processing window for preparing perovskite films.

We further set the temperature interval to 5 °C to investigate how the T-VAQ process affects perovskite films and device performance.

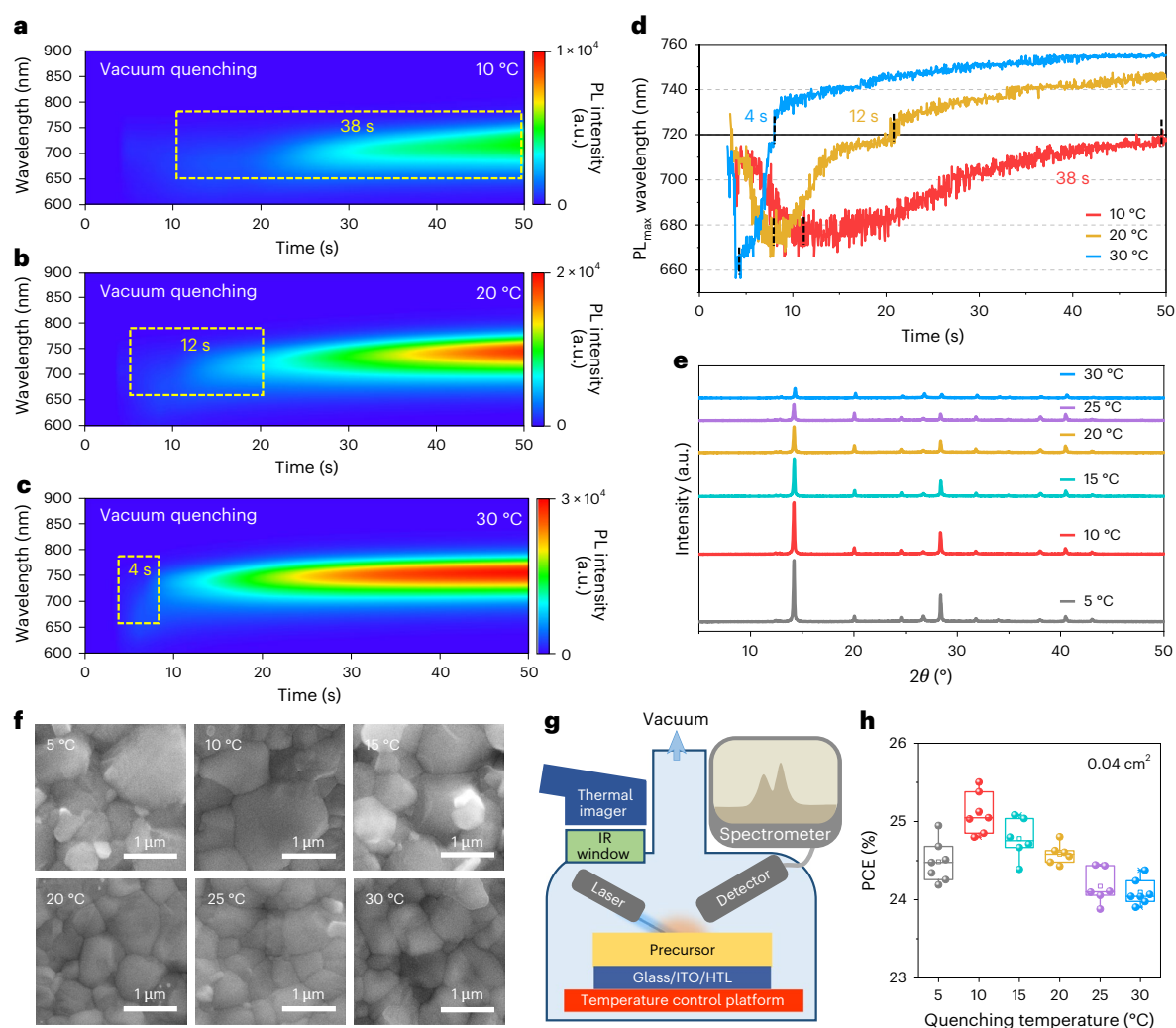


**Fig. 4 | Temperature-controlled vacuum quenching.** **a–c**, In situ photoluminescence heat map of perovskite film at 10 °C (**a**), 20 °C (**b**), or 30 °C (**c**) during vacuum quenching. **d**,  $PL_{max}$  wavelength of in situ photoluminescence versus time under different temperatures during the vacuum quenching process. **e**, XRD spectra of annealed perovskite films by vacuum quenching under different temperatures. **f**, SEM graph of annealed perovskite films by

vacuum quenching under different temperatures. **g**, Schematic diagram of the temperature control platform combined with in situ photoluminescence in the vacuum chamber. **h**, Statistical plots of PCE of PSCs on small areas obtained by vacuum quenching under different temperatures. Data from seven cells were statistically analysed. The box represents the median and quartiles, whereas the whiskers span the minimum to the maximum data points.

The T-VAQ treatment duration was adjusted for each temperature to ensure the photoluminescence peak wavelength shifted from 680 nm to 720 nm, maintaining the films within the same nucleation stage. Photographs of the intermediate phase films and the annealed films, processed at varying temperatures and durations, are presented in Supplementary Fig. 17. The intermediate phase films, obtained when the photoluminescence peak reached 720 nm, were expected to exhibit similar colours due to their identical photoluminescence peaks. However, they displayed a slightly darker appearance at higher temperatures, probably due to variations in quenching during the vacuum-breaking and vent periods. This continuous quenching process introduced subtle differences in the degree of quenching across the films. Nevertheless, the annealed films appeared visually similar to the naked eye (Supplementary Fig. 17c) and exhibited comparable photoluminescence spectra (Supplementary Fig. 18). By contrast, annealed perovskite films nucleated at lower temperatures showed larger grain sizes and enhanced XRD peaks (Fig. 4e,f). This observation may stem from suppressed nucleation and a slower transition from the intermediate phase to the perovskite phase at reduced temperatures. These conditions allow the intermediate phase more time to grow and facilitate uniform solute diffusion within the film. We fabricated

devices using these films to explore the impact of T-VAQ temperature on device performance. As shown in Fig. 4h, the PCE increases with decreasing T-VAQ temperature, peaking at 10 °C. Refer to Supplementary Fig. 19 and Supplementary Table 5 for details on additional device parameters. We attained similar results when we changed the solvent system to the mixed DMF–DMSO system: the low temperature could also open the processing window for the intermediate phases (Supplementary Fig. 20).

In addition to regulating the nucleation process, we adopted the additive (*p*-F-PEAI) strategy to further regulate the perovskite crystallization process to obtain higher-quality perovskite films. As shown in Supplementary Fig. 21, the perovskite film with *p*-F-PEAI additive reached the  $PL_{max}$  peak at 50 s after annealing. This was 14.5 s later than the control perovskite film, which reached the photoluminescence max peak after 35.5 s. In other words, the *p*-F-PEAI additive slowed down the crystallization rate of the perovskite film during annealing, resulting in a considerable increase in the grain size of the perovskite and a notable enhancement in crystallinity (from SEM and XRD in Supplementary Fig. 22). Based on the results of Fig. 3i and Supplementary Figs. 21 and 22, the *p*-F-PEAI additive can promote accelerated nucleation and slow crystallization, thereby obtaining higher-quality perovskite films.

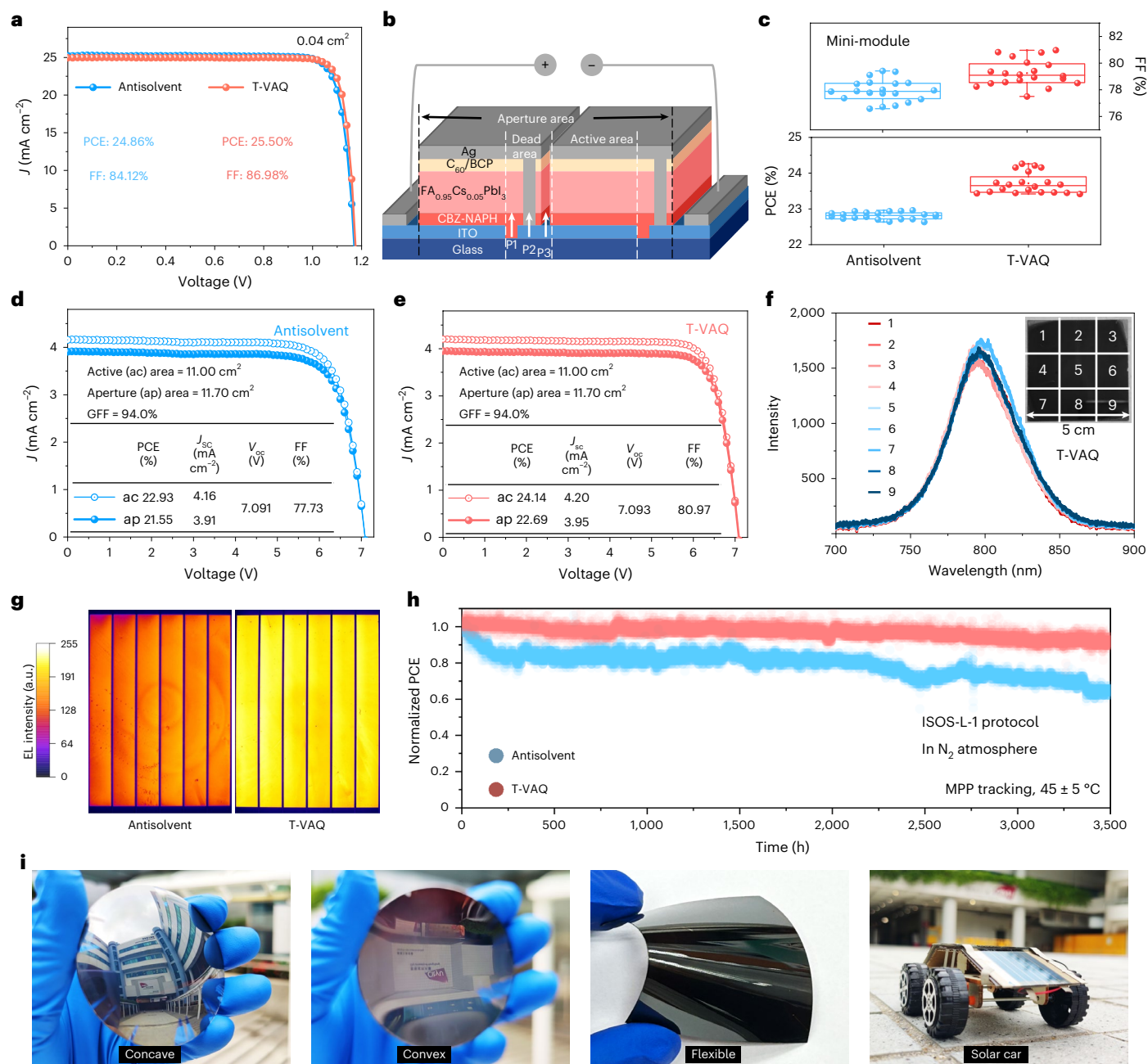


**Fig. 5 | Device characteristics.** **a**,  $J$ - $V$  curves of PSCs on small areas obtained by anti-solvent quenching and T-VAQ. **b**, Device architecture of the inverted perovskite mini-module. **c**, Statistical plots of the fill factor (FF) and PCE of PSMs obtained by anti-solvent quenching and T-VAQ. Data from 20 modules were statistically analysed. The box represents the median and quartiles, and the whisker covers the minimum up to the maximum data points. **d, e**,  $J$ - $V$  curves of PSMs obtained by anti-solvent quenching (d) and T-VAQ (e). GFF, geometric

fill factor. **f**, Photoluminescence measurement of different regions of the large-area perovskite film obtained by T-VAQ. The inset is a photograph of the perovskite film divided into nine regions. **g**, Electroluminescence mapping of the mini-modules obtained by anti-solvent and T-VAQ. **h**, Maximum power point tracking of unencapsulated PSCs under  $45 \pm 5^\circ \text{C}$  in  $\text{N}_2$ . **i**, Perovskite films on curved or flexible substrates, and on PSM-driven solar cars, which are treated by the T-VAQ method.

Furthermore, the shift of the Pb 4*f* and I 3*d* peaks shown by the X-ray photoelectron spectroscopy in Supplementary Fig. 23 confirms the interaction and potential passivation ability between the *p*-F-PEAI additive and the perovskite.

### Device characteristics

We fabricated inverted PSCs with an architecture of indium tin oxide (ITO)/self-assembled monolayer (SAM)/ $\text{FA}_{0.95}\text{Cs}_{0.05}\text{PbI}_3$ /piperazinium iodide/ $\text{C}_{60}$ /bathocuproine (BCP)/Ag (Supplementary Fig. 24) to evaluate the performance of the devices. As shown in Fig. 5a and Supplementary Figs. 25 and 26, small-area PSCs fabricated by the T-VAQ method

exhibited a superior PCE (25.50%) to those fabricated by anti-solvent quenching (24.86%). We also considered the upscaling capability of the T-VAQ method and successfully fabricated high-performance mini-modules (Fig. 5b). The statistical photovoltaic parameters of the mini-modules are summarized in Fig. 5c, Supplementary Fig. 27 and Supplementary Table 6; the target mini-modules based on the T-VAQ method exhibit an average PCE of 23.72%, which is higher than those based on anti-solvent quenching (22.81%). This improvement originated mainly from the enhancements to the fill factor and short circuit current density ( $J_{sc}$ ). The control mini-module prepared by anti-solvent quenching exhibited an active-area PCE of 22.93% with an active area of  $11.0 \text{ cm}^2$  (Fig. 5d).

By contrast, the mini-module prepared by the T-VAQ method exhibited a superior PCE of 24.14% (Fig. 5e), featuring a high fill factor of 80.97%, a  $V_{OC}$  of 7.093 V and  $aJ_{SC}$  of 4.20 mA cm<sup>-2</sup>. We also obtained the geometric fill factor of 94% on the mini-module through the step profiler (Supplementary Fig. 28 and Supplementary Table 7). The target mini-module therefore achieved an aperture-area PCE of 22.69% with an aperture area of 11.7 cm<sup>2</sup>. We then sent one of the mini-modules to an independent laboratory (Shanghai Institute of Microsystem and Information Technology, SIMIT, Shanghai, China) for certification, and a certified aperture-area PCE of 21.60% was obtained from the reverse  $J-V$  scan (Supplementary Fig. 29).

To explore the fundamental reasons for performance improvement, we initially compared the photoluminescence (Fig. 5f and Supplementary Fig. 28), ultraviolet–visible (UV–vis) absorption spectra (Supplementary Fig. 30) and SEM (Supplementary Fig. 31) of large-area perovskite films produced by anti-solvent quenching and T-VAQ, respectively. The films produced by T-VAQ exhibited much better uniformity than those obtained by anti-solvent quenching. We also evaluated the uniformity of large-area perovskite films using electroluminescence mapping. As shown in Fig. 5g, the T-VAQ device displays stronger overall electroluminescence intensity and superior uniformity, signifying improved film quality and reduced non-radiative recombination losses. The improved fill factor therefore primarily comes from more uniform nucleation and crystallization on large-area substrates based on T-VAQ. We also used a blade-coating method to address the inherent scalability and transferability issues of the spin-coating method. The results showed that the PSM prepared based on the T-VAQ method can still achieve high active-area PCE (23.1%) with an active area of 14.52 cm<sup>2</sup> (Supplementary Fig. 32), proving its feasibility for large-scale manufacturing. Moreover, this strategy was also applied to  $n-i-p$ -structured PSMs (Supplementary Fig. 33). A spin-coated  $n-i-p$  mini-module achieved a PCE of 21.18% and a blade-coated  $n-i-p$  mini-module achieved a PCE of 20.21% with an active area of 18 cm<sup>2</sup>. Furthermore, the strategy is also applicable to a 1.67 eV inverted wide-bandgap PSC with a PCE of 22.16%, demonstrating its potential in perovskite-based tandem solar cells (Supplementary Fig. 34).

The T-VAQ method ought to improve the stability of the perovskite films and solar cells. Hence we test the stability of the unencapsulated PSCs by following protocols established by the International Summit on Organic Photovoltaic Stability (ISOS)<sup>36</sup>. We examined the operational stability of the unencapsulated devices with maximum power point tracking under continuous 1-sun-equivalent white-light LED illumination at 45 °C in N<sub>2</sub> (Fig. 5h). The T-VAQ-based device retained approximately 93% of its initial PCE over 3,500 h. By contrast, the device with antisolvent quenching retained only 65% of its initial PCE after 3,500 h. Hence, our devices accomplished high efficiency and favourable operational stability, indicating that our T-VAQ method is efficacious. Furthermore, due to the isotropy of vacuum in T-VAQ, we successfully prepared mirror-like large-area perovskite films on convex, concave and flexible substrates (Fig. 5i), demonstrating the broader application of T-VAQ technology<sup>37,38</sup>. The mini-modules prepared by the T-VAQ method can drive the model solar vehicle along a rough road on cloudy days.

## Conclusion

In this study we employed in situ photoluminescence technology to uncover the variations in nucleation for three commonly used quenching nucleation processes. We then concentrated on vacuum quenching, dividing it into three stages and investigating the factors influencing each stage. We found that pumping speed, solvent systems (with different boiling points and donor numbers) and additives all have specific effects on nucleation related to the nature of the three stages of vacuum quenching. This discovery can offer valuable guidance for achieving high-quality nucleation through vacuum quenching. Notably, we developed the T-VAQ method by regulating the vacuum quenching

temperature. We discovered that a lower temperature can prolong the existence of the intermediate phase, thereby expanding the time window for subsequent processing, leading to high-quality, uniform and large-area perovskite films. The insights gained from this vacuum quenching nucleation research and the T-VAQ method will accelerate the large-scale production of more efficient perovskite solar modules.

## Online content

Any methods, additional references, Nature Portfolio reporting summaries, source data, extended data, supplementary information, acknowledgements, peer review information; details of author contributions and competing interests; and statements of data and code availability are available at <https://doi.org/10.1038/s41566-025-01703-3>.

## References

1. Fu, Q. & Jen, A. K. Y. Perovskite solar cell developments, what's next? *Next Energy* **1**, 100004 (2023).
2. Saki, Z., Byranvand, M. M., Taghavinia, N., Kedia, M. & Saliba, M. Solution-processed perovskite thin-films: the journey from lab- to large-scale solar cells. *Energy Environ. Sci.* **14**, 5690–5722 (2021).
3. Zhao, X. et al. Operationally stable perovskite solar modules enabled by vapor-phase fluoride treatment. *Science* **385**, 433–438 (2024).
4. Ding, B. et al. Dopant-additive synergism enhances perovskite solar modules. *Nature* **628**, 299–305 (2024).
5. Green, M. A. et al. Solar cell efficiency tables (Version 64). *Prog. Photovolt. Res. Appl.* **32**, 425–441 (2024).
6. Gao, H. et al. Homogeneous crystallization and buried interface passivation for perovskite tandem solar modules. *Science* **383**, 855–859 (2024).
7. Petrus, M. L. et al. Capturing the sun: a review of the challenges and perspectives of perovskite solar cells. *Adv. Energy Mater.* **7**, 1700264 (2017).
8. Goetz, K. P. & Vaynzof, Y. The challenge of making the same device twice in perovskite photovoltaics. *ACS Energy Lett.* **7**, 1750–1757 (2022).
9. Ternes, S. et al. Drying dynamics of solution-processed perovskite thin-film photovoltaics: in situ characterization, modeling, and process control. *Adv. Energy Mater.* **9**, 1901581 (2019).
10. Zhang, J. et al. Efficient and stable inverted perovskite solar modules enabled by solid–liquid two-step film formation. *Nano-Micro Lett.* **16**, 190 (2024).
11. Li, D. et al. A review on scaling up perovskite solar cells. *Adv. Funct. Mater.* **31**, 2008621 (2021).
12. Chen, S. et al. Stabilizing perovskite-substrate interfaces for high-performance perovskite modules. *Science* **373**, 902–907 (2021).
13. Taylor, A. D. et al. A general approach to high-efficiency perovskite solar cells by any antisolvent. *Nat. Commun.* **12**, 1878 (2021).
14. Li, X. et al. A vacuum flash-assisted solution process for high-efficiency large-area perovskite solar cells. *Science* **353**, 58–62 (2016).
15. Bishop, J. E. et al. High-efficiency spray-coated perovskite solar cells utilizing vacuum-assisted solution processing. *ACS Appl. Mater. Interfaces* **10**, 39428–39434 (2018).
16. Ternes, S. et al. Drying and coating of perovskite thin films: how to control the thin film morphology in scalable dynamic coating systems. *ACS Appl. Mater. Interfaces* **14**, 11300–11312 (2022).
17. Babayigit, A., D'Haen, J., Boyen, H.-G. & Conings, B. Gas quenching for perovskite thin film deposition. *Joule* **2**, 1205–1209 (2018).
18. Zeng, L. et al. Controlling the crystallization dynamics of photovoltaic perovskite layers on larger-area coatings. *Energy Environ. Sci.* **13**, 4666–4690 (2020).

19. Huang, C. et al. Meniscus-modulated blade coating enables high-quality  $\alpha$ -phase formamidinium lead triiodide crystals and efficient perovskite minimodules. *Joule* **8**, 2539–2553 (2024).
20. Ternes, S., Laufer, F. & Paetzold, U. W. Modeling and fundamental dynamics of vacuum, gas, and antisolvent quenching for scalable perovskite processes. *Adv. Sci.* **11**, 2308901 (2024).
21. Bi, L. et al. Deciphering the roles of MA-based volatile additives for  $\alpha$ -FAPbI<sub>3</sub> to enable efficient inverted perovskite solar cells. *J. Am. Chem. Soc.* **145**, 5920–5929 (2023).
22. Laufer, F. et al. Process insights into perovskite thin-film photovoltaics from machine learning with in situ luminescence data. *Sol. RRL* **7**, 2201114 (2023).
23. Schackmar, F. et al. In situ process monitoring and multichannel imaging for vacuum-assisted growth control of inkjet-printed and blade-coated perovskite thin-films. *Adv. Mater. Technol.* **8**, 2201331 (2023).
24. Szostak, R. et al. In situ and operando characterizations of metal halide perovskite and solar cells: insights from lab-sized devices to upscaling processes. *Chem. Rev.* **123**, 3160–3236 (2023).
25. Li, Z. et al. Scalable fabrication of perovskite solar cells. *Nat. Rev. Mater.* **3**, 18017 (2018).
26. Park, N.-G. & Zhu, K. Scalable fabrication and coating methods for perovskite solar cells and solar modules. *Nat. Rev. Mater.* **5**, 333–350 (2020).
27. Jiang, Z. et al. Solvent engineering towards scalable fabrication of high-quality perovskite films for efficient solar modules. *J. Energy Chem.* **80**, 689–710 (2023).
28. Du, M. et al. Surface redox engineering of vacuum-deposited NiO<sub>x</sub> for top-performance perovskite solar cells and modules. *Joule* **6**, 1931–1943 (2022).
29. Agresti, A., Di Giacomo, F., Pescetelli, S. & Di Carlo, A. Scalable deposition techniques for large-area perovskite photovoltaic technology: a multi-perspective review. *Nano Energy* **122**, 109317 (2024).
30. Liu, Y. et al. Controlled growth of uniform and dense perovskite layers on SnO<sub>2</sub> via interface passivation by PbS quantum dots. *EcoMat* **6**, e12456 (2024).
31. Liu, P., Tang, G. & Yan, F. Strategies for large-scale fabrication of perovskite films for solar cells. *Sol. RRL* **6**, 2100683 (2022).
32. Bu, T. et al. Dynamic antisolvent engineering for spin coating of 10×10 cm<sup>2</sup> perovskite solar module approaching 18%. *Sol. RRL* **4**, 1900263 (2020).
33. Khorasani, A., Mohamadkhani, F., Marandi, M., Luo, H. & Abdi-Jalebi, M. Opportunities, challenges, and strategies for scalable deposition of metal halide perovskite solar cells and modules. *Adv. Energy Sust. Res.* **5**, 2300275 (2024).
34. Antoine, C. Tensions des vapeurs; nouvelle relation entre les tensions et les températures. *CR Seances Acad. Sci.* **107**, 681–684 (1888). 778–780, 836–837.
35. Wang, Y. et al. Unlocking the ambient temperature effect on FA-based perovskites crystallization by in situ optical method. *Adv. Mater.* **36**, 2307635 (2024).
36. Khenkin, M. V. et al. Consensus statement for stability assessment and reporting for perovskite photovoltaics based on ISOS procedures. *Nat. Energy* **5**, 35–49 (2020).
37. Li, Z. et al. Surface-orientation elimination of vapor-deposited PbI<sub>2</sub> flakes for efficient perovskite synthesis on curved solar cells. *ACS Appl. Mater. Interfaces* **13**, 45496–45504 (2021).
38. Thornber, T. et al. Nonplanar spray-coated perovskite solar cells. *ACS Appl. Mater. Interfaces* **14**, 37587–37594 (2022).

**Publisher's note** Springer Nature remains neutral with regard to jurisdictional claims in published maps and institutional affiliations.

Springer Nature or its licensor (e.g. a society or other partner) holds exclusive rights to this article under a publishing agreement with the author(s) or other rightsholder(s); author self-archiving of the accepted manuscript version of this article is solely governed by the terms of such publishing agreement and applicable law.

© The Author(s), under exclusive licence to Springer Nature Limited 2025

## Methods

### Materials

All materials were used as received without further purification. Caesium iodide (CsI) and formamidinium iodide (FAI) were purchased from Greatcell (Australia). Lead iodide (PbI<sub>2</sub>) was purchased from TCI (Japan). Methylammonium chloride (MACl), fullerene 60 (C<sub>60</sub>) and BCP (purity of 99.9%) were purchased from Xi'an Polymer Light Technology Corporation (China). The solvents, including DMF, DMSO, NMP,  $\gamma$ -butyrolactone, 2-methoxyethanol, isopropanol and chlorobenzene (CB), were purchased from J&K (China). Silver was purchased from commercial sources with high purity. CbzNaph was synthesized as described in ref. 39.

### Substrate preparation

The ITO (15  $\Omega$  sq<sup>-1</sup>) glass substrates were patterned by a 532 nm laser. For 0.04 cm<sup>2</sup> cells, 1.5  $\times$  1.5 cm<sup>2</sup> ITO substrates were patterned into a 1.5  $\times$  1 cm<sup>2</sup> conducting surface. For the mini-module, 5  $\times$  5 cm<sup>2</sup> ITO substrates were patterned into 5 mm width sub-cells. For flexible ITO/PET substrates, the A4-sized substrates were cut into 5  $\times$  5 cm<sup>2</sup> shapes and stuck on the 5  $\times$  5 cm<sup>2</sup> glass substrate after cleaning. A  $\Phi$ 6 cm curved glass with an approximately 1 cm bulge was used for the curved substrates. All substrates were sequentially cleaned by sonication with detergent (Decon 90/deionized water with 1:4/v:v) for 2 h, followed by deionized water, acetone and IPA for 30 min, respectively. The cleaned ITO glass substrates were then transferred into an oven with a temperature of 80 °C.

### Hole transport layer preparation

The ITO was treated with low-pressure air plasma for 20 min before use. After plasma, within 1 h, 1.5 mg ml<sup>-1</sup> CbzNaph in CB:DMF (98.5:1.5)<sup>40</sup> was spin-coated onto the ITO glass substrate at 4,000 rpm for 30 s and was subsequently annealed at 100 °C for 10 min. After cooling to room temperature, the substrates are ready for perovskite precursor deposition.

### Precursor preparation

1. Precursor for spin-coated perovskite: the 1.4 M perovskite precursor solution was prepared by mixing 677.7 mg PbI<sub>2</sub>, 228.8 mg FAI and 18.2 mg CsI powder in 1 ml DMF:DMSO (4:1/v:v). The precursor was stirred overnight, 9.7 mg MACl and 10  $\mu$ l *p*-F-PEAI solution (100 mg ml<sup>-1</sup> in DMF) were added into the precursor to study the influence of additives on the nucleation process.
2. Precursor for blade-coated perovskite: the 0.9 M perovskite precursor solution was prepared by mixing 435.6 mg PbI<sub>2</sub>, 139.3 mg FAI and 11.7 mg CsI powder in 1 ml DMF:NMP (9:1/v:v). The precursor was stirred overnight, 6.1 mg MACl and 5  $\mu$ l *p*-F-PEAI solution (100 mg ml<sup>-1</sup> in DMF) were added into the precursor before coating.

### Fabrication of perovskite intermediate phase based on spin-coating method

Three nucleation methods are discussed as follows.

1. For the antisolvent quenching method, perovskite precursor solution (50  $\mu$ l) was dropped on the SAM and spin-coated at 2,000 rpm for 10 s and 5,000 rpm for 45 s. Chlorobenzene (180  $\mu$ l) as anti-solvent was quickly dripped onto the centre of perovskite film 5 s before the end of the spin-coating process. This resulted in a transparent yellow intermediate film. The process was performed in a N<sub>2</sub> glove box, with the air conditioning maintaining the temperature at 16–22 °C.
2. For the vacuum quenching method, 50  $\mu$ l of perovskite precursor solution was dropped on SAM and spin-coated at 2,000 rpm for 10 s and 5,000 rpm for 10 s. The resulting film was quickly transferred into the vacuum chamber.

The pressure will drop to lower 100 mTorr in 5 s. The precursor film was treated for 15 s to show a transparent yellow colour. The vacuum quenching process was carried out in an air glove box, with the relative humidity at 15–20% and the temperature at 22–25 °C.

In terms of pumping speed, all experiments, except for the one investigating the effect of pumping speed on the vacuum quenching process (which used a speed of 40 m<sup>3</sup> h<sup>-1</sup>), were conducted with a pump operating at 12 m<sup>3</sup> h<sup>-1</sup>. The pumping pressure requirement is generally to achieve a pressure of <10 Pa (or 75 mTorr) within 10 s of evacuating the chamber. In our study, a 12 m<sup>3</sup> h<sup>-1</sup> pump was used to evacuate a chamber of approximately 1 l, as illustrated by the pressure curves in Fig. 3b and Supplementary Fig. 8, which show a drop to <75 mTorr within 10 s.

Determining the optimal pumping time for achieving the best device performance depends on various factors such as differences in precursor systems, additives and substrates. We believe that the film needs to reach an appropriate intermediate phase; however, different systems may not achieve ideal efficiency at the same phase. We therefore recommend that other researchers experiment to identify the most suitable time for their specific systems. This time will vary with temperature, necessitating precise temperature control during vacuum quenching.

Regarding the optimal temperature for ideal device performance, we have found that, without affecting the tack time and while obtaining the desired intermediate phase, selecting a lower temperature can help produce films with higher orientation and larger grains, thereby enhancing device performance. However, researchers should tailor the specific temperature to their particular systems.

3. For the gas quenching method, 50  $\mu$ l of perovskite precursor solution was dropped on SAM and spin-coated at 2,000 rpm for 10 s and 5,000 rpm for 10 s. The resulting film was quickly transferred onto the suction platform. The air knife worked at 3 bar. The angle between the air knife and the substrate is about 45°. The distance between the air knife and the substrate is about 1 cm. The gas quenching process was conducted in an air glove box, with the relative humidity at 15–20% and temperature at 22–25 °C.

### Fabrication of perovskite intermediate phase based on blade-coating method

Three nucleation methods are discussed as follows.

1. For the antisolvent quenching method, 20  $\mu$ l of perovskite precursor solution was injected between the blade and the SAM substrates and the blade moved at 15 mm s<sup>-1</sup> with a gap of 100  $\mu$ m. The extra precursor was absorbed by the paper tissue attached at the end of the substrate. The prepared wet film was then immersed into a tank with 300 ml chlorobenzene as an anti-solvent. The process was performed in a dry air glove box, with the air conditioning maintaining the temperature at 22–25 °C and the relative humidity at 15–20%.
2. For the vacuum quenching method, 20  $\mu$ l of perovskite precursor solution was injected between the blade and the SAM substrates and the blade moved at 15 mm s<sup>-1</sup> with a gap of 100  $\mu$ m. The prepared wet film was transferred into the vacuum chamber. The pressure will drop to lower 100 mTorr in 5 s. The precursor film was treated for 15 s to show a transparent yellow colour. The vacuum quenching process was performed in an air glove box, with the relative humidity at 15–20% and the temperature at 22–25 °C.

- For the gas quenching method, 20  $\mu\text{l}$  of perovskite precursor solution was injected between the blade and the SAM substrates and the blade moved at  $15\text{ mm s}^{-1}$  with a gap of  $100\text{ }\mu\text{m}$ . The resulting film was quickly fixed onto the suction platform. The air knife worked on 3 bar. The angle between the air knife and the substrate is about  $45^\circ\text{C}$ . The distance between the air knife and the substrate is about 1 cm. The gas quenching process was carried out in an air glove box, with the relative humidity at 15–20% and temperature at  $22\text{--}25^\circ\text{C}$ .

The intermediate film was then annealed at  $100^\circ\text{C}$  for 30 min. Piperazinium iodide ( $0.25\text{ mg ml}^{-1}$  in IPA) is spin-coated on perovskite film at 4,000 rpm for 30 s and then annealed at  $100^\circ\text{C}$  for 10 min; 25 nm  $\text{C}_{60}$  was thermally evaporated on the film as ETL, then 6 nm BCP as a buffer layer, and 100 nm Ag as a current collector was thermally evaporated on the  $\text{C}_{60}$ . For the anti-reflection coating, an  $\text{MgF}_2$  layer with a thickness of 140 nm is thermally evaporated onto the back of the devices in the high vacuum chamber ( $<5 \times 10^{-6}$  Torr). The metal shadow mask with an aperture area of  $0.06\text{ cm}^2$  was used to determine the cell contact area. The perovskite solar cells were covered with a shading mask with an aperture area of  $0.04\text{ cm}^2$  to ensure the accuracy of current density from  $J$ - $V$  curves.

### Fabrication of PSMs

Perovskite solar modules with six subcells (5 mm width per cell) connected in series were fabricated on ITO glass with a  $5 \times 5\text{ cm}^2$  size. The series interconnection of the module was realized by P1, P2 and P3 lines, which were patterned using a laser scribing system with a wavelength of 532 nm and a power of 10 W (SCIPRIOS GmbH). The ITO substrate was pre-patterned for P1 (25  $\mu\text{m}$  wide) at 100% laser power and a speed of  $1,000\text{ mm s}^{-1}$ . The subsequent processes for the preparation of the SAM substrates, as well as the perovskite, piperazinium iodide and  $\text{C}_{60}$ /BCP layers, are the same as the small-area-device procedures. The P2 lines (125  $\mu\text{m}$  wide) were patterned with an average laser power of 65% at a speed of  $1,000\text{ mm s}^{-1}$ . After Ag layers were sequentially deposited, and the P3 lines (65  $\mu\text{m}$  wide) were patterned with an average laser power of 60% at a speed of  $200\text{ mm s}^{-1}$ . The distance between the P1 and P3 lines is about 300  $\mu\text{m}$  and the geometric fill factor is around 94%.

### Characterizations

The XRD patterns for perovskite film crystallization analysis are measured using a Bruker D2 Phaser with Cu K $\alpha$  radiation. Ultraviolet–visible absorption spectra were recorded on a UV–vis spectrometer (PerkinElmer model Lambda 2S). Photoluminescence was recorded by FLS980 spectrofluorometer (Edinburgh) with a xenon lamp and a pulsed excitation laser of 480 nm, respectively. The substrate for the photoluminescence measurement is non-conductive glass. The cross-sectional and top-view images of the samples were monitored by scanning electron microscopy (QUATTRO S).

### In situ photoluminescence measurements

In situ photoluminescence spectra were characterized by home-built equipment, including an excitation system, fibre system and detector system. The testing samples are held in a temperature-controlled  $\text{N}_2$  glove box or humidity-controlled air box with a fibre system set around the sample. By contrast, the excitation and detection system is set in the ambient environment and connected with the fibre. Excitation system using an excitation laser (315 nm, max = 30 W). Excitation light was introduced to the sample through a fibre. The emitted light from the sample was collected by fibre and introduced to a spectrophotometer (Ocean Optics USB2000). A 550 nm low pass filter is applied in the light pass to the spectrophotometer. The in situ photoluminescence system was integrated into (1) a spin-coater, (2) an antisolvent bath, (3) a vacuum quenching chamber and (4) an air knife platform, which was used to study the nucleation of the perovskite using different nucleation methods.

### Solar cell characterization

The  $J$ - $V$  characteristics of photovoltaic devices were measured in an  $\text{N}_2$ -filled glovebox at room temperature using a Keithley 2400 Source Meter under simulated sunlight from a solar simulator (EnliTech, SS-F5, Taiwan). A National Renewable Energy Laboratory-calibrated silicon solar cell (with a KG-2 filter) was used to obtain the AM 1.5G ( $100\text{ mW cm}^{-2}$ ) solar simulator's light intensity. The perovskite solar cells (perovskite solar modules) were covered with a shading mask with an aperture area of  $0.04\text{ cm}^2$  ( $11.70\text{ cm}^2$ ) to ensure the accuracy of the current density from the  $J$ - $V$  curves. Before  $J$ - $V$  measurements, a 140-nm-thick magnesium fluoride layer was deposited on the back of the ITO substrate to improve the transmittance. The  $J$ - $V$  measurements for the cells were conducted with sweep mode with reverse (from 1.20 V to  $-0.1$  V) and forward (from  $-0.1$  V to 1.20 V) scans with a scan step of 20 mV and a time delay of 100 ms. For modules, voltage was swept between 7.5 V to  $-0.1$  V with 0.1 V steps. The  $J$ - $V$  tests were conducted in a  $\text{N}_2$  glovebox. The external quantum efficiency for the cell was conducted using an external quantum efficiency measurement system (EnliTech, QE-R, Taiwan).

### Long-term device stability measurement

The solar cells were operated at their maximum power point tracking while being illuminated by a white LED source. The stability of the cells was monitored with a 91 PVKSOLAR MSCLT-1 automatic maximum power point tracker (1 sun illumination intensity of  $100\text{ mW cm}^{-2}$ ). Throughout the test, the sample chamber was maintained in ambient air with a continuous  $\text{N}_2$  flow.

### Reporting summary

Further information on research design is available in the Nature Portfolio Reporting Summary linked to this article.

### Data availability

The data that support the findings of this study are available from the corresponding authors on reasonable request. Source data are provided with this paper.

### References

- Jiang, W. et al.  $\pi$ -Expanded carbazoles as hole-selective self-assembled monolayers for high-performance perovskite solar cells. *Angew. Chem. Int. Ed.* **61**, e202213560 (2022).
- Liu, M. et al. Compact hole-selective self-assembled monolayers enabled by disassembling micelles in solution for efficient perovskite solar cells. *Adv. Mater.* **35**, 2304415 (2023).

### Acknowledgements

A.K.-Y.J. thanks the sponsorship of the Lee Shau-Kei Chair Professor (Materials Science), the City University of Hong Kong for the support from the APRC grants (grant nos. 9380086, 9610419, 9610440, 9610492 and 9610508), the Innovation and Technology Commission of Hong Kong for the MHKJFS (grant no. MHP/054/23), TCFS (grant no. GHP/121/22SZ) and MRP grants (grant no. MRP/040/21X), the Environment and Ecology Bureau of Hong Kong for the Green Tech Fund (grant no. 202020164), and the Research Grants Council of Hong Kong for the GRF (grant nos. 11304424, 11307621 and 11316422) and CRS grants (grant nos. CRS\_CityU104/23 and CRS\_HKUST203/23).

### Author contributions

L.B., Q.F. and A.K.-Y.J. conceived the idea. L.B. designed the equipment, fabricated the devices and conducted relevant characterizations. Q.F. designed the experimental protocol. J.W. and X.H. contributed to optimizing PSCs. X.J. and F.R.L. assisted in device preparation. Z.Z. and S.-W.T. conducted the in situ PL of antisolvent quenching characterization. A.K.-Y.J. and Q.F. supervised the project.

L.B. and Q.F. drafted the original manuscript, and Q.F. and A.K.-Y.J. finalized it. All authors contributed to data interpretation.

### Competing interests

The authors declare no competing interests.

### Additional information

**Supplementary information** The online version contains supplementary material available at <https://doi.org/10.1038/s41566-025-01703-3>.

**Correspondence and requests for materials** should be addressed to Qiang Fu or Alex K.-Y. Jen.

**Peer review information** *Nature Photonics* thanks Zhijun Ning and Yong Wang for their contribution to the peer review of this work.

**Reprints and permissions information** is available at [www.nature.com/reprints](http://www.nature.com/reprints).

## Solar Cells Reporting Summary

Nature Portfolio wishes to improve the reproducibility of the work that we publish. This form is intended for publication with all accepted papers reporting the characterization of photovoltaic devices and provides structure for consistency and transparency in reporting. Some list items might not apply to an individual manuscript, but all fields must be completed for clarity.

For further information on Nature Research policies, including our [data availability policy](#), see [Authors & Referees](#).

### ► Experimental design

Please check the following details are reported in the manuscript, and provide a brief description or explanation where applicable.

#### 1. Dimensions

Area of the tested solar cells	<input checked="" type="checkbox"/> Yes <input type="checkbox"/> No	<p>In our lab, the area of the solar cells tested is 4 mm<sup>2</sup> and the area for the solar module is 11.70 cm<sup>2</sup>. (Experimental procedures: Solar cell characterization).</p> <p><i>Explain why this information is not reported/not relevant.</i></p>
Method used to determine the device area	<input checked="" type="checkbox"/> Yes <input type="checkbox"/> No	<p>The active area of the cell, which was 5.3 mm<sup>2</sup>, is defined by the overlap of the ITO electrode and metal electrode. When we conduct the measurement, the area of the solar cells tested is defined by a non-reflective metal mask with an aperture area of 4 mm<sup>2</sup>. For the solar module, the area was determined by a metal mask with an aperture area of 11.70 cm<sup>2</sup>. (Experimental procedures: Solar cell characterization).</p> <p><i>Explain why this information is not reported/not relevant.</i></p>

#### 2. Current-voltage characterization

Current density-voltage (J-V) plots in both forward and backward direction	<input checked="" type="checkbox"/> Yes <input type="checkbox"/> No	<p>Forward and backward direction J-V scans were performed. (Supplementary Fig. 29)</p>
Voltage scan conditions	<input checked="" type="checkbox"/> Yes <input type="checkbox"/> No	<p>For the cells tested in our lab, the scan was performed in the range from -0.1 to 1.2 V, with a scan step of 0.02 V and dwell time of 10 ms. For the modules tested, the scan was performed in the range from -0.1 to 7.5 V, with a scan step of 0.1 V and dwell time of 10 ms.</p> <p><i>Explain why this information is not reported/not relevant.</i></p>
Test environment	<input checked="" type="checkbox"/> Yes <input type="checkbox"/> No	<p>For the cells tested in our lab, the cells were non-encapsulated and the measurements were performed in an N<sub>2</sub>-filled glove box at room temperature. For the certified cell, the cell was encapsulated and the measurements were carried out in ambient atmosphere at room temperature. Further details regarding test environment during certifications are provided in Experimental procedures: Solar cell characterization.</p> <p><i>Explain why this information is not reported/not relevant.</i></p>
Protocol for preconditioning of the device before its characterization	<input type="checkbox"/> Yes <input checked="" type="checkbox"/> No	<p><i>Provide a description of the protocol.</i></p> <p>No preconditioning protocol was applied.</p>
Stability of the J-V characteristic	<input checked="" type="checkbox"/> Yes <input type="checkbox"/> No	<p>We verified the stability of the J-V characteristics by monitoring the current output of the device at the maximum power-point voltage. (Fig. 5H)</p> <p><i>Explain why this information is not reported/not relevant.</i></p>

#### 3. Hysteresis or any other unusual behaviour

Description of the unusual behaviour observed during the characterization	<input type="checkbox"/> Yes <input checked="" type="checkbox"/> No	<p><i>Provide a description of hysteresis or any other unusual behaviour observed during the characterization.</i></p> <p>There is no unusual behaviour observed during the characterization, i.e., hysteresis.</p>
Related experimental data	<input type="checkbox"/> Yes <input checked="" type="checkbox"/> No	<p><i>Provide a description of the related experimental data.</i></p> <p>We are not reporting unusual behavior.</p>

## 4. Efficiency

External quantum efficiency (EQE) or incident photons to current efficiency (IPCE)

Yes  
 No

The EQE spectra were collected using an Enlitech QE-S EQE system equipped with a standard Si diode.

*Explain why this information is not reported/not relevant.*

A comparison between the integrated response under the standard reference spectrum and the response measure under the simulator

Yes  
 No

The values of the integrated current from EQE and the short-circuit current from J-V curve measured under AM 1.5G solar simulator are within 4% difference, which is within the accuracy confidence of the measurements.

*Explain why this information is not reported/not relevant.*

For tandem solar cells, the bias illumination and bias voltage used for each subcell

Yes  
 No

*Provide a description of the measurement conditions.*

We do not report tandem solar cells in this work.

## 5. Calibration

Light source and reference cell or sensor used for the characterization

Yes  
 No

In our lab, the cells were measured under AM 1.5G (100 mW cm<sup>-2</sup>) irradiation using an EnliTech SS-F5 solar simulator. The light intensity was calibrated using a silicon solar cell (with a KG-2 filter) from the National Renewable Energy Laboratory (Experimental procedures: Solar cell characterization).

*Explain why this information is not reported/not relevant.*

Confirmation that the reference cell was calibrated and certified

Yes  
 No

The solar simulator in our lab is equipped with a silicon solar cell (with a KG-2 filter) from the National Renewable Energy Laboratory (Methods section: Photovoltaic cells characterizations). For the certified cell, calibrated and certified reference cells were used.

*Explain why this information is not reported/not relevant.*

Calculation of spectral mismatch between the reference cell and the devices under test

Yes  
 No

*Provide a value of the spectral mismatch and/or a description of how it has been taken into account in the measurements.*

In our lab, the light spectrum matches well with the reference Si cell and we didn't calculate the spectral mismatch between the reference cell and the tested devices.

## 6. Mask/aperture

Size of the mask/aperture used during testing

Yes  
 No

For the cells tested in our lab, the mask/aperture area is 4 mm<sup>2</sup>. For the solar module, the mask aperture area is 11.70 cm<sup>2</sup>. (Experimental procedures: Solar cell characterization). For the module sent to certifications, the aperture area was defined as 11.7077 cm<sup>2</sup> (SIMIT, Supplementary Fig. 29).

*Explain why this information is not reported/not relevant.*

Variation of the measured short-circuit current density with the mask/aperture area

Yes  
 No

*Report the difference in the short-circuit current density values measured with the mask and aperture area.*

For the cells tested in our lab, all cells were measured using one identical mask.

## 7. Performance certification

Identity of the independent certification laboratory that confirmed the photovoltaic performance

Yes  
 No

One module was certified by the Shanghai Institute of Microsystem and Information Technology (SIMIT). (Supplementary Fig. 29)

*Explain why this information is not reported/not relevant.*

A copy of any certificate(s)

Yes  
 No

The copy of certificates are provided as Supplementary Fig. 29.

*Explain why this information is not reported/not relevant.*

## 8. Statistics

Number of solar cells tested

Yes  
 No

The information is provided in Supplementary Fig.26 and 27.

*Explain why this information is not reported/not relevant.*

Statistical analysis of the device performance

Yes  
 No

The information is provided in Fig. 5C and Supplementary Fig.26, 27.

*Explain why this information is not reported/not relevant.*

## 9. Long-term stability analysis

Type of analysis, bias conditions and environmental conditions

Yes

No

The statement of long-term stability test conditions is in Methods section and the information is shown in Figs. 5H.

*Explain why this information is not reported/not relevant.*